RSC Advances

PAPER

View Article Online
View Journal | View Issue



Cite this: *RSC Adv.*, 2017, **7**, 12446

# A simple spray reaction synthesis and characterization of hierarchically porous $SnO_2$ microspheres for an enhanced dye sensitized solar cell†

Hui Zhang,*[a] Rong Wu,[a] Hong Xu,[a] Fan Li,*[b] Shuo Wang,[a] Jinshu Wang*[c] and Tingting Zhang[a]

Received 23rd November 2016
Accepted 9th February 2017

DOI: 10.1039/c6ra27235e

rsc.li/rsc-advances

This paper reports first on the novel synthesis of hierarchical tin dioxide ($SnO_2$) porous microspheres in the absence of a template using a simple spray reaction technique and annealing at 500–800 °C. The $SnO_2$ microspheres obtained are tetragonal phase and approximately 2.2–2.7 μm in diameter, and they consist of 6.7–23.1 nm crystallites and possess hierarchical pores and Brunauer–Emmett–Teller (BET) surface areas of up to 55 $m^2$ $g^{-1}$. Using ultraviolet-visible absorption spectra analysis, it is found that $SnO_2$ crystallites demonstrate a quantum size effect, resulting in a widening of the band gap of the $SnO_2$ spheres. This band gap can be tuned from 3.99 eV (800 °C) to 4.26 eV (600 °C) by varying the annealing temperature. Using separated $SnO_2$ porous spheres as the scattering layer of the photoanode for dye sensitized solar cells (DSSCs), the solar light-electricity conversion efficiency (maximum: 6.0%) is increased by up to 31.9% and 28.2% compared to cells using a commercial $SnO_2$ powder and P25 nanopowder as the scattering layers, respectively, under the same conditions.

## 1. Introduction

Dye sensitized solar cells (DSSCs) are one of the promising alternatives to the currently dominant, commercial bulk silicon-based solar cells because of their simple production process, low cost, and increasingly improved power conversion efficiency (PCE),[1–3] which has recently been reported to be as high as 12% under AM1.5 irradiation.[3] The performance of DSSCs is primarily determined by the light harvesting efficiency (LHE), the quantum yield for charge injection and the efficiency of collecting the injected charges at the back contact.[4] The material selection and the microstructure design for the photoanode, such as the material's physical and chemical properties and morphology, are critical for obtaining the previously mentioned cell performances.[5] Conventionally, titanium dioxide ($TiO_2$) nanocrystals that are approximately 20 nm in diameter are the most commonly used anode material for DSSCs.[6–8] Compared with $TiO_2$, tin dioxide ($SnO_2$) is an n-type semiconductor and has a wider band gap ($SnO_2$: 3.6 eV; $TiO_2$: 3.2 eV) and a higher electron mobility ($SnO_2$: 125–250 $cm^2$ $V^{-1}$ $s^{-1}$; $TiO_2$: 0.1–1.0 $cm^2$ $V^{-1}$ $s^{-1}$).[9–11] The larger band gap for $SnO_2$ can create fewer oxidative holes in the valence band, which is favorable to the long-term stability of DSSCs.[12] The higher electron mobility of $SnO_2$ can give a faster electron diffusion rate which facilitates the transport of photogenerated carriers. Furthermore, $SnO_2$ with a high refractive index of 2.0 is also suitable for application in the scattering layer to increase the LHE and the ultimate conversion efficiency of photons to electrons as a result of the Mie scattering effect. In addition, $SnO_2$ also has other very important energy storage applications such as in lithium ion batteries and so on.[13]

However, $SnO_2$-based DSSCs have exhibited a low conversion efficiency of solar light to electricity.[14–17] Morphologically and structurally diverse $SnO_2$-based materials for use as the photoanode of DSSCs have been synthesized, and the cells display enhanced conversion efficiencies.[18–26] Among those materials, porous and hollow microspheres are both significant structures that have a high specific area and strong reflecting and scattering of incident light. The conversion efficiency of $SnO_2$ DSSCs based on these two types of nanostructure has exceeded 5%.[19] $SnO_2$-based porous and hollow spheres are normally prepared *via* the template route.[27] Recently, the molten salt process and solid state reaction process without using an organic template have been applied to synthesize nano-$SnO_2$ and other metal oxide nanomaterials.[28,29] These processes are simple, the purity of product is high, and the size of product is controlled.

[a]School of Science, Beijing Jiaotong University, Beijing 100044, PR China. E-mail: hzhang1@bjtu.edu.cn

[b]College of Environmental and Energy Engineering, Beijing University of Technology, Beijing 100124, PR China. E-mail: vanadiumli@bjut.edu.cn

[c]College of Materials, Beijing University of Technology, Beijing 100124, PR China. E-mail: wangjsh@bjut.edu.cn

† Electronic supplementary information (ESI) available. See DOI: 10.1039/c6ra27235e

Compared with both of these processes, the advantage of using a spray reaction (SR) process is being able to obtain fairly spherical shaped materials. In this paper, the synthesis and characterization of high surface area $SnO_2$ microspheres with hierarchically porous structure using a novel SR process is reported.[30] The prepared $SnO_2$ porous spheres reveal that a broadened and tuned band gap is obtained by changing the annealing temperature. DSSCs made from $SnO_2$ porous spheres as the scattering layer of the anode with a pre-coated $TiO_2$ nanocrystalline thin film yield the highest PCE of 6.0% under standard AM1.5 conditions, which increases to 31.9% and 28.2%, when compared to the commercial $SnO_2$ powder and $TiO_2$ nanoparticles (P25 nanopowder) DSSCs, respectively. This is because of the porous spheres' dual functionality of providing efficient light scattering and high dye loading.[16]

## 2. Experimental

Tin tetrachloride ($SnCl_4$) and chloroplatinic acid ($H_2PtCl_6$) were purchased from the Sinopharm Chemical Reagent Co., Ltd. The ammonia cylinder was acquired from Beijing Huayuan Gas Co., China. Ethyl cellulose was acquired from Aladdin (Shanghai) Co., Ltd. $TiO_2$ nanopowder (P25), ruthenium dye (N719, chemical formula: ruthenium(2,2-bipyridyl-4,4-dicarboxylate)$_2$(NCS)$_2$ where NCS = *N*-chlorosuccinimide), electrolyte (DHS-E23, which is composed of 1,2-dimethyl-3-propylimidazolium iodide, guanidine thiocyanate, lithium iodide, tributyl phosphate, iodine, and acetonitrile), and bare fluorine doped tin oxide (FTO) conducting glasses and ones with a 12 μm thickness, 0.36 $cm^2$ square area transparent $TiO_2$ nanocrystalline film (labeled FTO–$TiO_2$) were all purchased from Dalian Rainbow Light Solar Technology Development Co., China. Commercial $SnO_2$ powder with an average particle diameter of 8 μm was purchased from the Yunnan Tin Group (Holding) Company Limited.

$SnO_2$ porous spheres were, for the first time, synthesized using a SR process proposed previously by our group, and the detailed procedure is described elsewhere.[30,31] Briefly, a 30 wt% $SnCl_4$ aqueous solution was first atomized in the aerosol generator. Then, aerosols of the tin salt solution were reacted with ammonia ($NH_3$) gas from the $NH_3$ cylinder in the reactor, to form the $SnO_2$ precursor spherical particles which were collected into the collector (see schematic of the synthesis setup in Fig. S1; ESI†). Next, $SnO_2$ precursor spheres were washed several times with distilled water and washed twice with anhydrous ethanol and then dried at low power for 12 min in a microwave oven. Finally, the precursor spheres were calcined in air at 500 °C, 600 °C, 700 °C, or 800 °C for 2 h. The process undergoes the reactions as follows:

$$NH_3 \xrightarrow{\text{colliding}} Sn^{4+} \text{ solution droplets} \quad (1)$$

$$NH_3 + H_2O \rightleftharpoons NH_3 \cdot H_2O \quad (2)$$

$$NH_3 \cdot H_2O \rightleftharpoons NH_4 + OH^- \quad (3)$$

$$Sn^{4+} + OH^- \rightleftharpoons Sn(OH)_4\downarrow \quad (4)$$

$$Sn(OH)_4 \xrightarrow{\Delta} SnO_2 + H_2O\uparrow \quad (5)$$

To obtain microspheres of less than 600 nm size, $SnO_2$ spheres were separated using Stokes' equation:

$$\mu = \frac{(\rho_s - \rho_f) g D^2}{18\mu} \quad (6)$$

where $\mu$ is the sphere's settling velocity (m $s^{-1}$), $\rho_s$ is the mass density of the sphere (kg $m^{-3}$), $\rho_f$ is the mass density of the dispersing fluid (kg $m^{-3}$), $g$ is the gravitational acceleration (m $s^{-2}$), $D$ is the diameter of the sphere (m), and $\eta$ is the dynamic viscosity (N s $m^{-2}$).

The scattering layer paste was first prepared by adding 0.1 g of separated $SnO_2$ microspheres or $SnO_2$ powder or P25 powder and 0.375 g ethyl cellulose to 3 ml ethanol, mixing the mixture under ultrasonic vibration for 20 min and then grinding it for 20 min. The paste obtained was coated with a doctor blade onto the transparent $TiO_2$ layer of FTO–$TiO_2$ glass or the bare FTO glass as anode. Then, the film was sintered at 450 °C for 30 min. The total thickness of the film including the $TiO_2$ nanocrystalline layer was approximately 20 μm.

The $TiO_2$–$SnO_2$ and $TiO_2$–$TiO_2$ bilayered and the $SnO_2$ single-layered electrodes were each immersed in $3 \times 10^{-4}$ M N719 ethanol solution for 12 h. All the counter electrodes were fabricated by depositing 30 drops of 5 mM $H_2PtCl_6$ solution onto a 3 $cm^2$ bare FTO conducting glass and then calcining it at 350 °C for 15 min. After the anodes and cathodes were assembled into cells, one drop of DHS-E23 electrolyte solution was injected into the cell from the gap between anode and cathode and allowed to penetrate inside the bilayer film *via* capillary action. All the cell sizes were close to 0.36 $cm^2$. The DSSCs with photoanodes of $SnO_2$ spheres calcined at 500 °C, 600 °C, 700 °C, or 800 °C, and together with the commercial $SnO_2$ powder, and the P25 powder used as scattering layers, were named TS500, TS600, TS700, TS800, TCS, and TP25, respectively. The cell labeled S600 was fabricated using pure 600 °C $SnO_2$ spheres as anode without a $TiO_2$ nanocrystalline bottom layer. The cell labeled T was assembled with a commercial $TiO_2$ photoanode (FTO–$TiO_2$). The cells S600 and T have an approximately 10 μm thick semiconductor film.

The morphology and size of the $SnO_2$ spheres were determined using a scanning electron microscope (SEM) (Zeiss Supra 55). The average size of the spheres was estimated by counting 200 spheres from representative SEM images of the samples. The pore structure and specific surface area of porous $SnO_2$ microspheres were characterized using a nitrogen ($N_2$) adsorption apparatus (Micrometritics ASAP 2010). The microstructure of the spheres was observed using a transmission electron microscope (TEM) (Jeol JEM-2010). The crystalline phase in the spherical powders was identified using X-ray powder diffraction (XRD) (Bruker D8 ADVANCE) with Cu K$\alpha_1$ irradiation ($\lambda$ = 0.15406 nm). The chemical component and bonding on the surface of the $SnO_2$ spheres were determined using X-ray photoelectron spectroscopy (XPS) (ULVAC-PHI PHI 5000 VersaProbe II) using a Al K$\alpha$ irradiation ($h\nu$ = 1486.6 eV) as excitation source. Fourier-transform infrared (FTIR) spectra of

samples were recorded on an IR spectrometer (Bruker Vector 22) with a potassium bromide pellet. Raman spectra of $SnO_2$ microspheres were obtained using a confocal laser microRaman spectrometer (HORIBA Jobin Yvon HR800). Both optical absorption and diffuse reflection properties of $SnO_2$ spheres were measured on a spectrometer (Shimadzu UV-3100) with an integrating sphere as an accessory. Photoluminescence (PL) characteristics of $SnO_2$ spheres were examined using a fluorescence spectrometer (PerkinElmer LS 55) with a 275 nm excitation wavelength from an aqueous dispersion of $SnO_2$ particles. Photoelectrochemical measurements were conducted with a potentiostat (Princeton Applied Research EG&G 273) under AM1.5 irradiation from a 500 W xenon lamp.

## 3. Results and discussion

As observed from the SEM micrographs (Fig. 1(a–d)), $SnO_2$ particles heated at 500–800 °C were similar in appearance to the zirconium oxide ($ZrO_2$) microspheres obtained using the SR technique,[30,31] and were quite spherical in shape and possessed three analogous types of porous structure, that is, homogeneous, loose core/dense shell, and hollow structure. The formation process of these three structures is briefly discussed in the fourth paragraph of this section. The average diameter of the spheres is found to vary from 2.7 μm (standard deviation: 0.9 μm) to 2.2 μm (standard deviation: 0.6 μm) in a temperature range of 500–800 °C. With an increasing calcination temperature, the diameter of the sphere reduces, and the sphere breakage is exacerbated because of the rapid release of $H_2O$ gas generated by the decomposition of tin hydroxide ($Sn(OH)_4$) in inhomogeneously structured spheres.[30] The surface of some spheres also flakes, resulting from the stress produced by the heat shrink difference between the surface and the interior of each sphere.

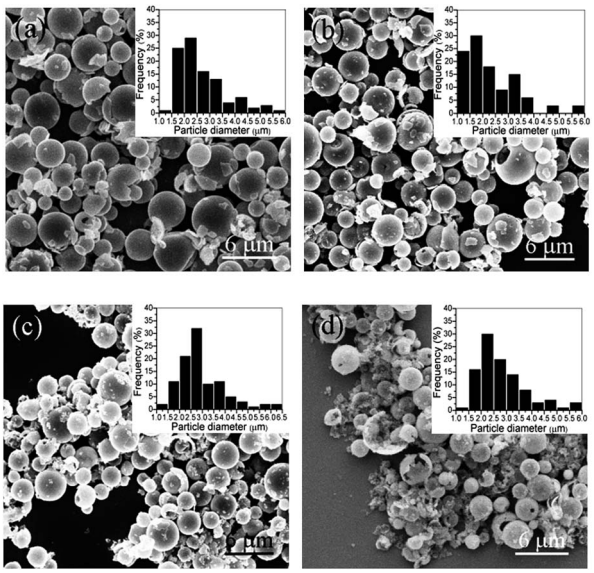


Fig. 1 SEM images and size distributions of $SnO_2$ microspheres calcined at (a) 500 °C, (b) 600 °C, (c) 700 °C, and (d) 800 °C.

XRD patterns (Fig. 2(a)) of $SnO_2$ spherical powders calcined at 500–800 °C reveal that all of the diffraction peaks are indexed to a tetragonal structure (JCPDS no. 41-1445). The grain size can be calculated using Scherrer's formula based on the full width at half maximum of the three most intense diffraction peaks (Table 1). With the calcination temperature rising from 500 to 800 °C, the grain size increases. This widespread grain growth phenomenon has been explained previously.[32] The Rietveld refined XRD data of the $SnO_2$ samples are shown in Fig. S3 (ESI†) and Table 1. The fitted lattice parameter values for the samples annealed at 600–800 °C agree well with the reported results in a paper by Baur,[33] but all the values of lattice parameter "*a*" are less and the values of lattice parameter "*c*" are greater than those reported by Reddy *et al.*,[28] and this is caused by the different synthesis process of $SnO_2$. Compared to the samples annealed at 600–800 °C, the 500 °C sample's "*a*" value is small and its "*c*" value is large probably because of the poor crystallinity of $SnO_2$.

Results of the Raman analysis of $SnO_2$ porous spheres were in good agreement as well (Fig. 2(b)). According to group theory, the normal lattice vibrations of tetragonal $SnO_2$ at the $\Gamma$ point of the Brillouin zone can be expressed as follows:

$$\Gamma = 1A_{1g} + 1A_{2g} + 1A_{2u} + 1B_{1g} + 1B_{2g} + 2B_{1u} + 1E_g + 3E_u \quad (7)$$

where $A_{1g}$, $B_{1g}$, $B_{2g}$, and $E_g$ are the Raman active modes. In Fig. 2(b) three Raman peaks appear at 475–481 $cm^{-1}$, 633–636 $cm^{-1}$, and 775–781 $cm^{-1}$, corresponding to $E_g$, $A_{1g}$, and $B_{2g}$ vibration modes, respectively. These three Raman modes confirm the tetragonal crystalline structure. Whereas another

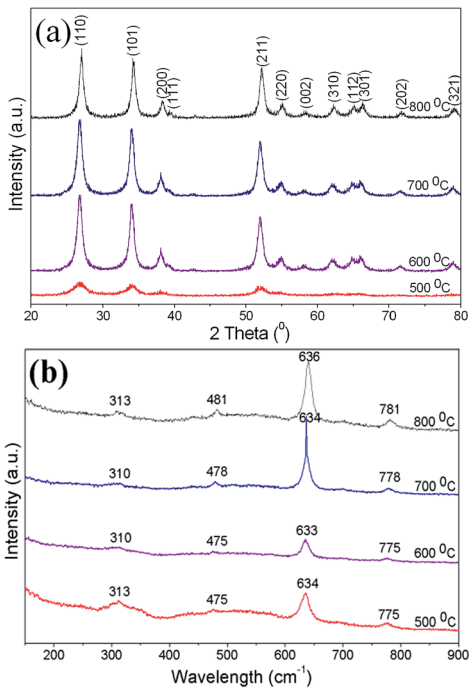


Fig. 2 (a) XRD patterns and (b) Raman spectra of $SnO_2$ spherical powders obtained at 500–800 °C.

Table 1 Properties of $SnO_2$ porous spheres

| Calcination temperature (°C) | Sphere diameter (μm) | Crystalline phase | Average crystallite size (radius, nm) | Lattice parameter | | BET surface area ($m^2\ g^{-1}$) | $E_g^{eff}$ (eV) | |
|---|---|---|---|---|---|---|---|---|
| | | | | $a$ (Å) | $c$ (Å) | | Cal. | Exp. |
| 500 | 2.7 | Tetragonal | 3.35 | 4.728 | 3.193 | 55 | 3.72 | — |
| 600 | 2.5 | Tetragonal | 5.30 | 4.738 | 3.188 | 47 | 3.65 | 4.26 |
| 700 | 2.3 | Tetragonal | 6.45 | 4.740 | 3.189 | 22 | 3.63 | 4.00 |
| 800 | 2.2 | Tetragonal | 11.6 | 4.736 | 3.185 | 14 | 3.61 | 3.99 |

Raman mode at 310–313 $cm^{-1}$ is probably associated to the surface defect in the crystallites or to the nanocluster formation in the $SnO_2$ microspheres.[34]

The formation mechanism of hierarchical $SnO_2$ porous microspheres, as illustrated in Fig. 3, is similar to that of the $ZrO_2$ microspheres prepared *via* the SR route, which has been discussed in depth in previous publications.[30,31] Schematically, atomized $SnCl_4$ solution droplets collided with $NH_3$ molecules, and $Sn^{4+}$ precipitation occurred from the surface to the interior of the droplets, thus forming the $SnO_2$ precursor, $Sn(OH)_4$, spheres consisting of $Sn(OH)_4$ nanoparticles. The completely reactive droplets produced homogenously structured $Sn(OH)_4$ spheres. After $Sn(OH)_4$ spheres were annealed, $SnO_2$ porous microspheres with a uniform structure consisting of $SnO_2$ nanocrystals and mesopores were generated because of $H_2O$ loss. Both loose core/dense shell and hollow $SnO_2$ spheres originated from the precursor spheres with similar structures, which were largely formed from both larger $SnCl_4$ solution aerosols and aerosols that were suspended in the upper section of the reactor. Such aerosols were not able to precipitate fully because of their short residence time in the reactor.

Fig. 4(a) is a typical SEM photograph of a close observation of $SnO_2$ microspheres heated at 500–800 °C, from which it can be clearly observed that hierarchical $SnO_2$ porous spheres are composed of nanocrystals, mesopores among the nanocrystals, and hollow macropores in incomplete-reaction spheres. To further determine the microstructure of the spheres, TEM characterization was carried out. All the samples annealed at 500–800 °C have similar TEM results, as shown in Fig. 4(a and b). The inset in Fig. 4(a) is a representative TEM microphotograph of nanocrystals consisting of $SnO_2$ spheres, which demonstrate that the grains have square, spherical, and hexagonal shapes. The mesopores among the nanocrystals are irregularly shaped. The inset in Fig. 4(b) is the selected area electron diffraction (SAED) pattern of the nanocrystals shown in the inset of Fig. 4(a), which is similarly determined to be tetragonal $SnO_2$ (t-$SnO_2$), and this is consistent with the XRD result. The high-resolution TEM (HRTEM) image (Fig. 4(b)) of the $SnO_2$ grains clearly displays the formation of t-$SnO_2$ with (110) and (101) planes.

The $N_2$ adsorption/desorption isotherm profiles (Fig. 5) for the samples obtained at 500–800 °C show a type III isotherm with a large type H3 hysteresis loop according to the IUPAC classification. The Brunauer–Emmett–Teller (BET) specific surface area (Fig. S4; ESI†) can reach 55 $m^2\ g^{-1}$ for the 500 °C sample, and it decreases with an increase in annealing temperature from 500 °C to 800 °C because the pore size shrinks and some of the pores even close. Compared with the porous spheres synthesized using the template method and the nano-$SnO_2$ (BET surface area: 83 $m^2\ g^{-1}$) prepared using the molten salt method,[28] the less specific surface area of our samples is because of the larger diameter of the spheres and the closing of some of the pores in the shell during heating. Table 1 summarizes the properties of $SnO_2$ porous spheres calcined in the temperature range from 500–800 °C.

In order to study the surface composition and chemical state of the porous $SnO_2$ microspheres, XPS characterization was

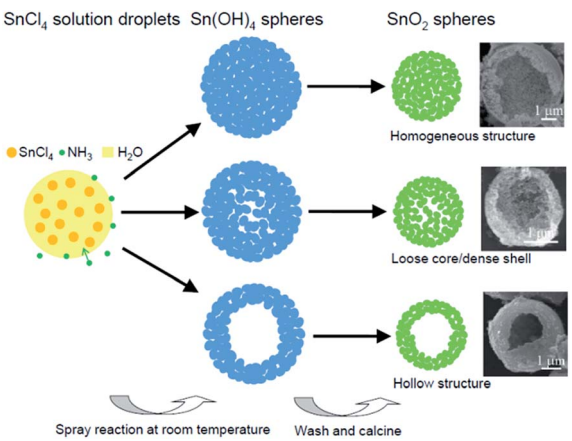


Fig. 3 Schematic illustration of the formation process of hierarchical $SnO_2$ porous microspheres.

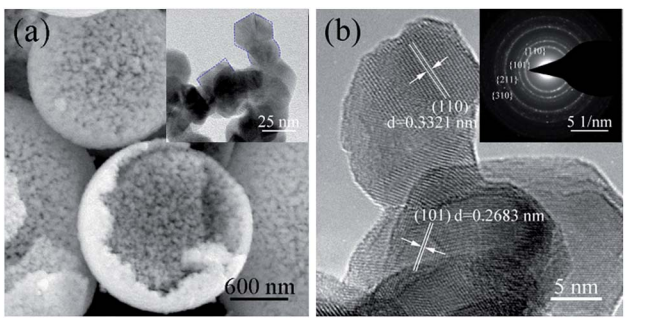


Fig. 4 (a) High magnification SEM image of representative $SnO_2$ porous spheres and typical TEM photograph (inset) of $SnO_2$ crystallites; (b) HRTEM micrograph and SAED pattern (inset) of $SnO_2$ crystallites.

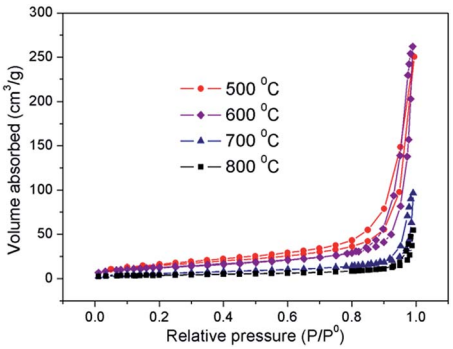


Fig. 5 $N_2$ adsorption/desorption isotherms of $SnO_2$ microspheres heated at 500–800 °C.

carried out. Fig. 6 illustrates the HRXPS spectra of Sn 3d and O 1s as well as the survey spectra for the $SnO_2$ spheres heated at 500–700 °C. The survey spectra show that the surfaces of all the $SnO_2$ spheres only contain Sn and O elements. All the samples demonstrate a spin–orbit doublet of Sn 3d at ~487 eV ($3d_{5/2}$) and ~495 eV ($3d_{3/2}$).[35] Meanwhile, after the O 1s peaks were fitted with Gaussian–Lorentzian functions, the main peak of O 1s at ~531 eV was assigned to the lattice oxygen, and the shoulder peak corresponded to the oxygen in the Sn–OH bond. The integrated intensity ratio of $OH^-/O^{2-}$ reduces with the increase of calcination temperature because of the decrease of hydroxyl groups resulting from the growth of crystallites and the diminishing of the surface area. The binding energies of Sn and O elements are close to those found in previous reports in the literature.[36]

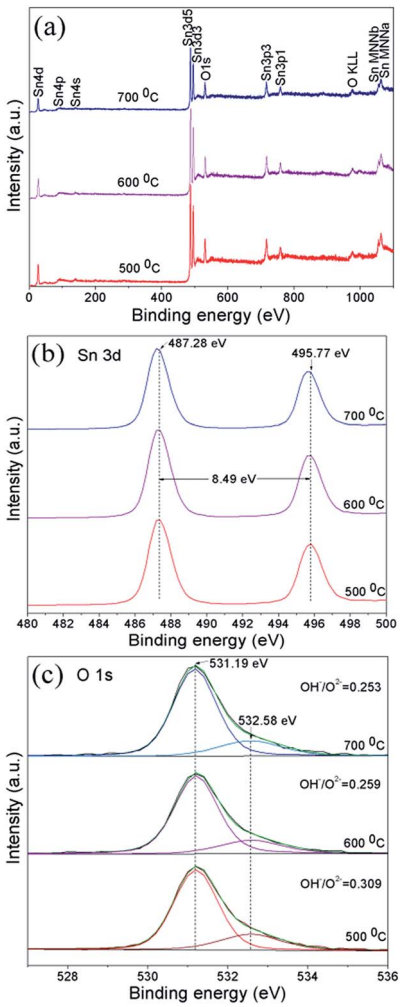


Fig. 6 (a) Survey, (b) Sn 3d, and (c) O 1s XPS spectra measured for $SnO_2$ spheres annealed at 500–700 °C.

In DSSCs, the binding mode of dye molecules on the semiconductor surface is quite significant for the photogenerated electrons' transfer and even the cell efficiency. For this reason, the FTIR spectra of the samples were examined. Essentially, the FTIR spectrum of the pure $SnO_2$ spheres calcined at 500 °C was recorded and exhibited several bands or peaks (Fig. 7(a)) as follows: bands at 527 $cm^{-1}$ [$\nu$(Sn–O, terminal)], 599 $cm^{-1}$ [$\nu$(Sn–O)], and 733 $cm^{-1}$ [$\nu_{as}$(Sn–O–Sn)], bands at 963 $cm^{-1}$, 1069 $cm^{-1}$, 1114 $cm^{-1}$, and 1382 $cm^{-1}$ assigned to lattice vibrations, a peak at 1258 $cm^{-1}$ [$\delta$ OH(Sn–OH, terminal)], a band centered around 1645 $cm^{-1}$ [$\delta$ OH($H_2O$)], two peaks at 2926 $cm^{-1}$ and 2964 $cm^{-1}$ [$\nu$(OH···O, bridged)], two bands at 2854 $cm^{-1}$ and 3406 $cm^{-1}$ [$\nu$ OH(Sn–OH, bridged)].

In order to acquire the adsorption information of the N719 molecules on the $SnO_2$ surface, FTIR spectral examinations were conducted for the N719 dye adsorbed on the film coated with 500 °C calcined $SnO_2$ porous spheres and the dye adsorbed on P25 film for comparison, marked as N719–S500 and N719–P25, respectively (Fig. 7(b)). Obviously, the intensity of most of

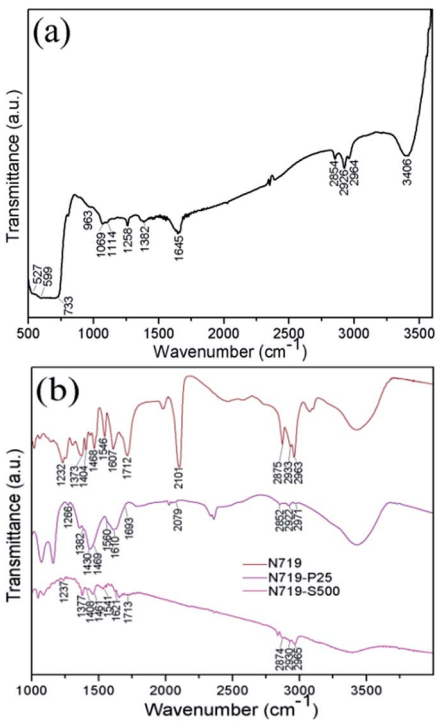


Fig. 7 IR spectra of (a) $SnO_2$ porous spheres calcined at 500 °C and (b) N719 molecules adsorbed on P25 and the $SnO_2$ spheres calcined at 500 °C.

the same bands dramatically reduces in the order of pure N719, N719–P25 to N719–S500. This means that N719 molecules bind stronger to $TiO_2$ than to $SnO_2$ because $SnO_2$ has a relatively weak adsorption to the dyes with acidic carboxyl anchoring groups.[25] It is generally believed that N719 molecules are bound to the oxide semiconductor surface through the anchoring of the carboxylic acid and carboxylate groups in three ways: unidentate mode, chelating mode, and bridging bidentate mode.[37] The specific binding mode can be determined using the Deacon–Phillips rule by calculating the $\Delta\nu$ between the asymmetric ($\nu_{as}$) and symmetric ($\nu_s$) stretching modes of the carboxylate unit, namely, $\Delta\nu = \nu_{as}(COO^-) - \nu_s(COO^-)$. The Deacon–Phillips rule is: $\Delta\nu$(unidentate) > $\Delta\nu$(ionic form) ≈ $\Delta\nu$(bidentate bridging) > $\Delta\nu$(bidentate chelating). Applying the $\Delta\nu$ criterion, the anchoring mode between N719 and $SnO_2$ may be unidentate whereas the type of bonding between N719 and P25 is probably bridging. However, this conclusion needs to be further confirmed by other analysis techniques, such as Raman and X-ray absorption spectroscopy and so on.

As a photoanode material, the optical property of $SnO_2$ porous microspheres is of paramount importance. Firstly the light scattering property of the samples was investigated using a diffuse reflection spectrum measurement. As shown in Fig. 8(a), with an increase in calcination temperature, the scattering capability of porous $SnO_2$ spheres is enhanced as the average diameter of the $SnO_2$ spheres becomes smaller. According to Mie theory, when the particle size is close to or larger than the wavelength of incident light, the smaller the particle size is, the more intense the light scattering of the particles is. With increasing calcination temperature, the average diameter of $SnO_2$ spheres reduces. Thus, the 800 °C sample has the most intense light scattering.

The absorption spectra (Fig. 8(b)) show that when the annealing temperature is elevated, the absorption intensity of the $SnO_2$ spheres enlarges in the visible region because the light scattering capability of the spheres is enhanced. The $SnO_2$ absorption edge was determined using the differential function from the differential absorption maximum (Fig. 8(c)). According to the formula of absorption edge ($\lambda = 1240/E_g$),[38] the absorption edge of bulk $SnO_2$ appears at around 344 nm in the absorption spectrum. In comparison with bulk $SnO_2$, the absorption edges of the $SnO_2$ porous spheres have blue-shifted to 311 nm ($E_g$: 3.99 eV), 310 nm ($E_g$: 4.0 eV), and 291 nm ($E_g$: 4.26 eV) for the samples annealed at 800 °C, 700 °C, and 600 °C, respectively. These result from the quantum size effect of crystallites which constitute the $SnO_2$ spheres. With a decrease of the annealing temperature and the resultant reduction of dimension of the crystallites, the absorption edge blue-shifts towards a shorter wavelength.[39] Therefore, the band gap of the $SnO_2$ porous spheres is tailorable just by varying the annealing temperature alone. The band gap energy of $SnO_2$ samples (Part 2 in the ESI†) was also calculated approximately. The calculated band gaps (Table 1) present a similar trend to the calcination temperatures but are less than the experimental values, caused by both the approximate equation (eqn (1) in ESI†) and the effect of ethanol (Fig. S6; ESI†).

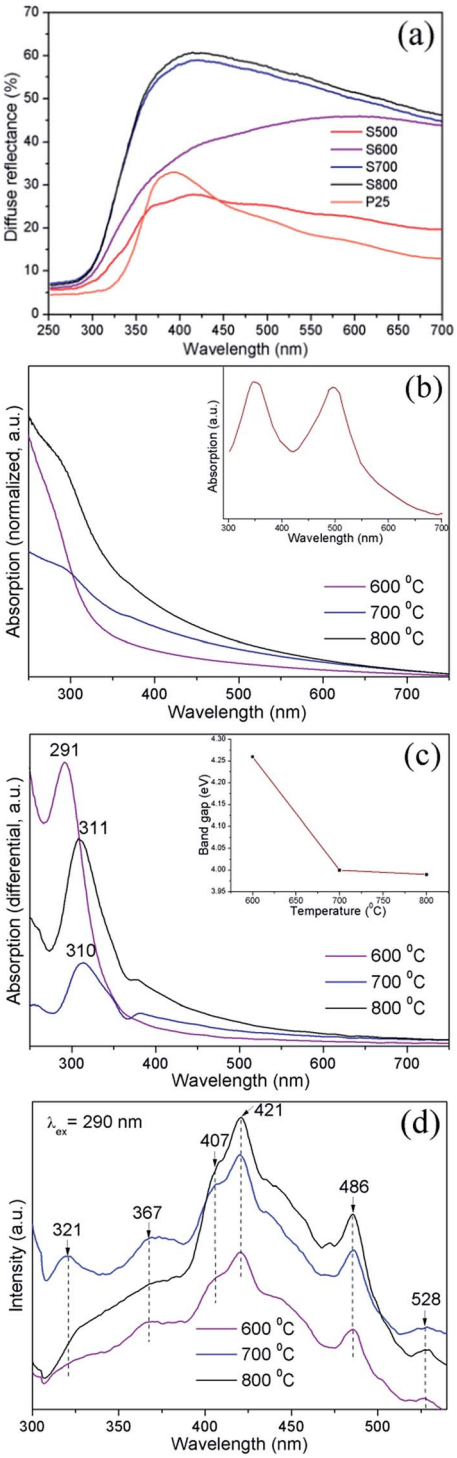


Fig. 8 (a) Diffuse reflections of $SnO_2$ porous microspheres annealed at 500–800 °C and P25 powder; (b) UV-Visible (UV-Vis) absorption spectra of both the ethanol dispersions of $SnO_2$ porous spheres annealed at 600–800 °C and a 25 μM N719 standard solution (inset) and (c) the corresponding differential absorption spectra of $SnO_2$ spheres; (d) PL spectra of $SnO_2$ porous spheres annealed at 600–800 °C.

The PL characteristics of the material are closely related to its optical absorption property. The PL spectra of $SnO_2$ microspheres were obtained from 300 nm to 540 nm with an

excitation wavelength ($\lambda_{ex}$) of 290 nm, as shown in Fig. 8(d). It can be noted that with an increase of annealing temperature, the PL intensity of $SnO_2$ spheres was enhanced in the wavelength range from 400 nm to 500 nm as a result of the reinforced light absorption of the spheres. In all the samples, the PL spectra exhibited three ultraviolet (UV) emission peaks centered at 321 nm (3.86 eV), 367 nm (3.38 eV), and 407 nm (3.05 eV) and three visible emission peaks at around 421 nm (2.95 eV), 486 nm (2.55 eV), and 528 nm (2.35 eV). These six emission energies are distinctly all lower than the deduced band gaps. Two UV emissions at 321 nm and 367 nm are attributed to the free-exciton recombination. The rest of the emission peaks come from the recombination of the excitons trapped in different defect states in the band gap with holes in the valence band. The defect states are generally formed by oxygen vacancies in the $SnO_2$ surface, the presence of which was verified by the Raman mode at around 310 $cm^{-1}$. In $SnO_2$, the oxygen vacancies have three kinds of charge state: $V_O^0$, $V_O^+$, and $V_O^{++}$, among which the 528 nm emission peak is generated by single oxygen vacancies ($V_O^+$). The PL peaks in all the samples calcined at 600–800 °C do not shift visibly with increasing calcining temperature as they have similar band gaps.

Fig. 9(a) displays the current–voltage ($I$–$V$) characteristics of DSSCs under standard AM1.5 irradiation, and the related photovoltaic parameters are listed in Table 2. It can be seen that the cell TS500 shows the highest short-circuit current density ($J_{sc}$) and PCE and the highest open-circuit voltage ($V_{oc}$) and fill factor (FF) in all DSSCs presented here. For cells TS500–TS800, the scattering capability and the dye loading, both of which determine $J_{sc}$ (Fig. S7; ESI†), and the FF present a more linear relationship with the calcination temperature of $SnO_2$ because these three values strongly depend on the size, pore diameter and surface area of the $SnO_2$ porous spheres. Consequently, the $J_{sc}$ and the PCE, because of similar $V_{oc}$, also exhibit a linear trend as well with the calcination temperature (Table 2). Normally, the PCE tracks linearly with the $J_{sc}$ (Fig. 9(b)) and the $J_{sc}$ and PCE also tracks linearly with the dye loading (Fig. 9(c)). For cells TCS, TP25, T, and S600, because of the distinct material composition and structure of the anodes, the efficiency does not track linearly with the $J_{sc}$ (Fig. 9(b)) and the $J_{sc}$ and efficiency do not track linearly with the dye loading either (Fig. 9(c)). The previous phenomena will be discussed more in the following sections.

For cells TS500–TS800, with the decrease of calcination temperature, the amount of dye loading increases, which results from the enlarged surface area of the $SnO_2$ spheres and directly results in the increase of $J_{sc}$. It is seen that cell TS500 yields the highest PCE of 6.0% because of its superior photoelectrochemical performance with a $J_{sc}$ of 13.02 mA $cm^{-2}$, a $V_{oc}$ of 0.73 V, and the FF of 63.03%. Compared with the remaining cells, the higher PCE of cell TS500 is attributed to the increased $J_{sc}$ and FF. The high $J_{sc}$ value for cell TS500 most likely results from a large amount of dye absorption because of a high surface area as well as the enhanced light harvesting that is brought out by the multiple light reflections and scatterings within the $TiO_2$/$SnO_2$ bilayer. The improvement in the FF value of TS500 cell is caused by the higher porosity of $SnO_2$ layer than those for the

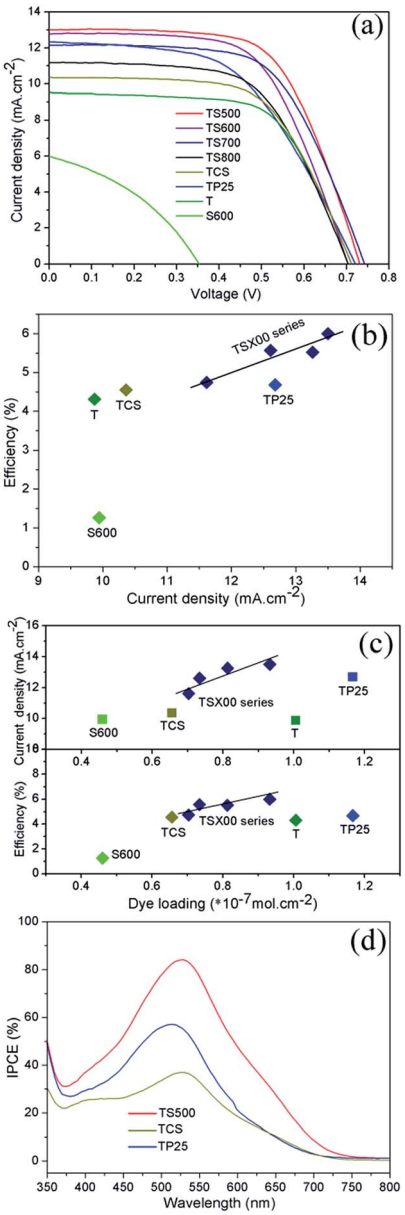


Fig. 9 (a) $I$–$V$ curves, (b) comparison of efficiency with current density, and (c) comparisons of efficiency and current density with dye loading for cells TS500–TS800, TCS, TP25, T, and S600. (d) Incident photon-to-current conversion efficiency (IPCE) of cells TS500, TCS, and TP25.

TS600–TS800 cells, leading to suppressed back electron transfer or a lower internal resistance in the bilayered photoanode. Meanwhile, compared with cell TS600, the PCE value for cell TS700 is slightly higher because of its larger $V_{oc}$ and FF values, which is probably because of the unstable test. Additionally, the effect of photoanode film thickness (17.5 μm, 20 μm, and 25 μm) was studied using 600 °C $SnO_2$ spheres as a scattering layer. The performance parameters of cells (Fig. S8; ESI†) show that the cell with a 20 μm thick anode has optimal efficiency thanks to it having the highest $J_{sc}$ and the intermediate FF of the three thickness cells. The cell of 17.5 μm thickness has the largest FF and the lowest $J_{sc}$, resulting from the thinner anode and the lower dye loading and light scattering intensity, which results in

 

Table 2 Photovoltaic characteristics for bilayered DSSCs with different diameter $SnO_2$ porous spheres acting as scattering layers

| Cells | Total film thickness (μm) | Active area ($cm^2$) | Normalized scattering capability of $SnO_2$ and P25[a] (%) | Dye loading ($\times 10^{-7}$ mol $cm^{-2}$) | $J_{sc}$ (mA $cm^{-2}$) | $V_{oc}$ (V) | FF (%) | $\eta$ (%) |
|---|---|---|---|---|---|---|---|---|
| TS500 | 20 | 0.36 | 34.3 | 0.932 | 13.02 | 0.73 | 63.03 | 6.00 |
| TS600 | 20 | 0.36 | 59.2 | 0.813 | 12.79 | 0.70 | 61.29 | 5.52 |
| TS700 | 20 | 0.36 | 74.9 | 0.734 | 12.16 | 0.74 | 61.67 | 5.57 |
| TS800 | 20 | 0.36 | 76.8 | 0.703 | 11.20 | 0.70 | 60.11 | 4.74 |
| TCS | 20 | 0.36 | — | 0.656 | 10.36 | 0.71 | 61.69 | 4.55 |
| TP25 | 20 | 0.36 | 29.8 | 1.167 | 12.23 | 0.72 | 52.61 | 4.68 |
| T | 10 | 0.36 | — | 1.006 | 9.52 | 0.71 | 63.61 | 4.31 |
| S600 | 10 | 0.36 | 59.2 | 0.460 | 9.59 | 0.21 | 37.41 | 1.26 |

[a] Obtained by calculating the integrated area under each diffuse reflection curve in Fig. 8(a).

the lowest efficiency. For the 25 μm thick cell with the second highest efficiency, its FF is the lowest among the three cells because of the thicker anode, and its $J_{sc}$ is less than that of the 20 μm thick cell possibly because of electron hole recombination.

As the scattering layer of DSSC photoanode, the light scattering property of $SnO_2$ porous spheres will directly influence the cell's LHE. The optical absorption of $SnO_2$ spheres will generate the photoelectrons that could not transfer to $TiO_2$ because of the lower conduction band edge of $SnO_2$ than $TiO_2$. The PL property of $SnO_2$ spheres is helpful to improve the cell's LHE, but that emitted light is relatively weak and contributes less to LHE. Thus, in the optical property of $SnO_2$ porous spheres, only the light scattering effect is crucial to enhance the performance of the DSSCs. Fig. 8(a) and Fig. 9(a–c) demonstrate that the light scattering intensity of $SnO_2$ porous spheres is enhanced with the increase of calcination temperature whereas the efficiency of DSSCs decreases. This illustrates again that the enhanced photovoltaic performance of cells lies on the increased amount of dye loading because of the high surface area of $SnO_2$ porous spheres as well as the strong light scattering effect.

The performances of the cells with the prepared $SnO_2$ porous spheres, the commercial $SnO_2$ particles, and the commercial $TiO_2$ nanoparticles as anode scattering layers, and the cell with pure $SnO_2$ porous spheres as anode material were also compared. Compared with cells TCS and TP25, the PCEs of cells TS500–TS800 were enhanced by as much as 31.9% and 28.2%, respectively, because of the increased $J_{sc}$ and FF. The excellent photovoltaic property of cells which have $SnO_2$ porous spheres as the scattering layer is largely because of the improved LHE as a result of multiple light scatterings and reflections off the $SnO_2$ hierarchically porous structure, faster electron mobility in $SnO_2$ than in $TiO_2$, and suppressed back electron transfer in the bilayered photoanode because the conduction band edge of intrinsic $SnO_2$ is 0.3 eV more positive than that of $TiO_2$. For cell S600, its lower photon-to-electron conversion efficiency is mainly because of the weak adsorption of the $SnO_2$ surface to N719 dye with acidic groups, the recombination of the electrons in the $SnO_2$ conduction band with the oxidized dye, and the low $V_{oc}$ caused by the $SnO_2$ Fermi energy level.[25] The limitations mentioned previously are inherent in $SnO_2$-based DSSCs. The cell T, used only for comparison purposes, demonstrates a normal photovoltaic performance of $TiO_2$ DSSC.

Fig. 9(d) presents the incident photon-to-current conversion efficiency (IPCE) spectra of cells TS500, TCS and TP25 in the wavelength range from 350 nm to 800 nm. The IPCE results are consistent with the $J_{sc}$ values of the cells, showing high quantum efficiencies at around 525 nm and 518 nm, respectively. In particular, the maximum IPCE reached as high as 84% for the TS500 cell. Compared to cells TCS and TP25, the increase of IPCE for cell TS500 is primarily attributed to the $SnO_2$ hierarchically porous microstructure both absorbing more dye and forming an intense light scattering layer in the photoanode.

## 4. Conclusions

Without using any templating agent, the hierarchical $SnO_2$ porous microspheres with high surface area were, for the first time, synthesized using the SR technique after calcining in the temperature range from 500 °C to 800 °C. The $SnO_2$ spheres obtained were thoroughly characterized using SEM, TEM, XRD, Raman spectroscopy, FTIR, XPS, and $N_2$ adsorption/desorption isotherm analyses. Furthermore the optical characteristics of $SnO_2$ porous spheres were also determined as well. The results obtained illustrate that the synthesized $SnO_2$ porous spheres composed of around 6.7–23.1 nm grains were all tetragonal $SnO_2$, less than 2.7 μm in diameter, and up to 55 $m^2 g^{-1}$ in BET surface area. UV-Vis absorption spectrum analysis revealed that $SnO_2$ grains present a quantum size effect, which broadened the band gap of the $SnO_2$ spheres. The band gap was able to be tuned from 3.99 eV (800 °C) to 4.26 eV (600 °C) by varying the calcining temperature. Additionally, this was the first time that $SnO_2$ porous spheres synthesized using the SR technique were utilized as a light scattering layer for a DSSC photoanode. Using $TiO_2$ nanocrystalline film as the bottom layer of the photoanode, DSSCs were assembled and achieved a maximum PCE improvement of 39.1% and 28.2% (the highest efficiency: 6.0%) compared to the cells fabricated with the commercial $SnO_2$ powder and P25 nanopowder as scattering layers, respectively, under the same processing conditions. The enhanced photoelectric conversion efficiency was primarily because of the high surface area of $SnO_2$ hierarchically porous microspheres, which results in both the intense light scattering and reflection effects and the adsorption of a large number of dye molecules on the $SnO_2$ surface.

## Acknowledgements

This work was supported financially by the National Science Foundation of China (Grant No. 51474014, 51471006, 51472009, 51534009, 51225402, 51172007). We thank Dr Yutao Ma for his helpful discussion.

## References

1 B. O'Regan and M. Grätzel, *Nature*, 1991, **353**, 737–740.
2 P. N. Zhu, Y. Z. Wu, M. V. Reddy, N. A. Sreekumaran, S. J. Peng, N. Sharma, V. K. Peterson, B. V. R. Chowdari and S. Ramakrishna, *RSC Adv.*, 2012, **2**, 5123–5126.
3 A. Yella, H. W. Lee, H. N. Tsao, C. Y. Yi, A. K. Chandiran, M. K. Nazeeruddin, E. W. G. Diau, C. Y. Yeh, S. M. Zakeeruddin and M. Grätzel, *Science*, 2011, **334**, 629–634.
4 J. K. Lee and M. J. Yang, *Mater. Sci. Eng., B*, 2011, **176**, 1142–1160.
5 A. Le Viet, R. Jose, M. V. Reddy, B. V. R. Chowdari and S. Ramakrishna, *J. Phys. Chem. C*, 2010, **114**, 21795–21800.
6 Y. Yoshida, S. Tokashiki, K. Kubota, R. Shiratuchi, Y. Yamaguchi, M. Kono and S. Hayase, *Sol. Energy Mater. Sol. Cells*, 2008, **92**, 646–650.
7 P. V. V. Jayaweera, A. G. U. Perera and K. Tennakone, *Inorg. Chim. Acta*, 2008, **361**, 707–711.
8 S. Yahav, S. Ruhle, S. Greenwald, H.-N. Barad, M. Shalom and A. Zaban, *J. Phys. Chem. C*, 2011, **115**, 21481–21486.
9 J. Chen, C. Li, F. Xu, Y. D. Zhou, W. Lei, L. T. Sun and Y. Zhang, *RSC Adv.*, 2012, **2**, 7384–7387.
10 V. Ganapathy, E. H. Kong, Y. C. Park, H. M. Jang and S. W. Rhee, *Nanoscale*, 2014, **6**, 3296–3301.
11 G. L. Shang, J. H. Wu, M. L. Huang, J. M. Lin, Z. Lan, Y. F. Huang and L. Q. Fan, *J. Phys. Chem. C*, 2012, **116**, 20140–20145.
12 A. Birkel, Y. G. Lee, D. Koll, X. V. Meerbeek, S. Frank, M. J. Choi, Y. S. Kang, K. Char and W. Tremel, *Energy Environ. Sci.*, 2012, **5**, 5392–5400.
13 M. V. Reddy, G. V. S. Rao and B. V. R. Chowdari, *Chem. Rev.*, 2013, **113**, 5364–5457.
14 X. C. Dou, D. Sabba, N. Mathews, L. H. Wong, Y. M. Lam and S. Mhaisalkar, *Chem. Mater.*, 2011, **23**, 3938–3945.
15 M. A. Hossain, G. W. Yang, M. Parameswaran, J. R. Jennings and Q. Wang, *J. Phys. Chem. C*, 2010, **114**, 21878–21884.
16 P. N. Zhu, M. V. Reddy, Y. Z. Wu, S. J. Peng, S. Y. Yang, N. A. Sreekumaran, K. P. Loh, B. V. R. Chowdari and S. Ramakrishna, *Chem. Commun.*, 2012, **48**, 10865–10867.
17 S. H. Ahn, D. J. Kim, W. S. Chi and J. H. Kim, *Adv. Mater.*, 2013, **25**, 4893–4897.
18 J. Y. Liu, T. Luo, T. S. Mouli, F. L. Meng, B. Sun, M. Q. Li and J. H. Liu, *Chem. Commun.*, 2010, **46**, 472–474.
19 Y. F. Wang, K. N. Li, C. L. Liang, Y. F. Hou, C. Y. Sua and D. B. Kuang, *J. Mater. Chem.*, 2012, **22**, 21495–21501.
20 S. Gubbala, V. Chakrapani, V. Kumar and M. K. Sunkara, *Adv. Funct. Mater.*, 2008, **18**, 2411–2418.
21 J. F. Qian, P. Liu, Y. Xiao, Y. Jiang, Y. L. Cao, X. P. Ai and H. X. Yang, *Adv. Mater.*, 2009, **21**, 3663–3667.
22 M. Liu, J. Y. Yang, S. L. Feng, H. Zhu, J. S. Zhang, G. Li and J. Y. Peng, *New J. Chem.*, 2013, **37**, 1002–1008.
23 Y. F. Wang, J. W. Li, Y. F. Hou, X. Y. Yu, C. Y. Su and D. B. Kuang, *Chem.–Eur. J.*, 2010, **16**, 8620–8625.
24 T. T. Duong, H. J. Choi, Q. J. He, A. T. Le and S. G. Yoon, *J. Alloys Compd.*, 2013, **561**, 206–210.
25 H. K. Wang and A. L. Rogach, *Chem. Mater.*, 2014, **26**, 123–133.
26 C. T. Gao, X. D. Li, B. A. Lu, L. L. Chen, Y. Q. Wang, F. Teng, J. T. Wang, Z. X. Zhang, X. J. Pan and E. Q. Xie, *Nanoscale*, 2012, **4**, 3475–3481.
27 K. N. Li, Y. F. Wang, Y. F. Xu, H. Y. Chen, C. Y. Su and D. B. Kuang, *ACS Appl. Mater. Interfaces*, 2013, **5**, 5105–5111.
28 M. V. Reddy, Y. T. Lee, K. Z. B. Wen and B. V. R. Chowdari, *Mater. Lett.*, 2015, **138**, 231–234.
29 A. K. Jibin, M. V. Reddy, G. V. Subba Rao, U. V. Varadaraju and B. V. R. Chowdari, *Electrochim. Acta*, 2012, **71**, 227–232.
30 H. Zhang, Z. T. An, F. Li, Q. Tang, K. Lu and W. C. Li, *J. Alloys Compd.*, 2008, **464**, 569–574.
31 H. Zhang, H. Lu, Y. W. Zhu, F. Li, R. G. Duan, M. Zhang and X. D. Wang, *Powder Technol.*, 2012, **227**, 9–16.
32 C. V. Thompson, *Annu. Rev. Mater. Sci.*, 1990, **20**, 245–268.
33 W. H. Baur, *Acta Crystallogr.*, 1956, **9**, 515–520.
34 K. Vijayarangamuthu and S. Rath, *J. Alloys Compd.*, 2014, **610**, 706–712.
35 S. Gubbala, H. B. Russell, H. Shah, B. Deb, J. Jasinski, H. Rypkema and M. K. Sunkara, *Energy Environ. Sci.*, 2009, **2**, 1302–1309.
36 M. V. Reddy, N. Sharma, S. Adams, R. R. Prasada, V. K. Peterson and B. V. R. Chowdari, *RSC Adv.*, 2015, **5**, 29535–29544.
37 A. Hagfeldt, G. Boschloo, L. C. Sun, L. Kloo and H. Pettersson, *Chem. Rev.*, 2010, **110**, 6595–6663.
38 C. L. Li, J. Yuan, B. Y. Han and W. F. Shangguan, *Int. J. Hydrogen Energy*, 2011, **36**, 4271–4279.
39 X. X. Xu, J. Zhuang and X. Wang, *J. Am. Chem. Soc.*, 2008, **130**, 12527–12535.

 